Comparative Thermal Analysis of Single and Double Channel Cold Plates for LiFePO4 Battery Modules

Manuscript received January 26, 2026; revised May 10, 2026

Mohamad Yamin*
Department of Mechanical Engineering
Gunadarma University
Jakarta, Indonesia
mohay@staff.gunadarma.ac.id

Aldi Gufroni
Department of Mechanical Engineering
Gunadarma University
Jakarta, Indonesia
gufronialdi44@gmail.com

Aniekan Elijah Asukwo
Department of Electrical Engineering
Modibbo Adama University
Yola, Nigeria
aaelijah@mau.edu.ng

***Abstract*— Li-ion batteries provide many advantages and are essential components of energy-storage systems for electric automobiles. A crucial aspect of battery operation is the maintenance of optimal temperature levels, which necessitate the implementation of a robust battery thermal management system. This study assessed the efficacy of two cold-plate configurations, a single parallel channel and a double parallel channel, in regulating the temperature of a 7 Ah LiFePO4 battery module comprising of three cells. Employing ANSYS 2023 R1 Academic License, a numerical analysis was performed to evaluate their performance. A battery discharge rate of 5C was used to investigate the changes in the mass flow rates ranging from 0.001 to 0.005 kg/s. The cooling fluid and ambient temperatures were maintained at 25°C. This study shows that double parallel-channel cold plates can be more effective than single parallel-channel cold plates in reducing battery module temperatures. Additionally, the use of double parallel-channel cold plates can result in a lower cooling fluid pressure drop. In addition, the cooling fluid used in the double parallel channel cold plate had a lower heat-transfer coefficient and Nusselt number.**

Keywords*— CFD, Cold Plate, Electric Vehicle, LiFePO4, Parallel Channel.

I. INTRODUCTION

Electric vehicles (EVs) are increasingly deployed to reduce greenhouse-gas emissions associated with fossil-fuel transportation by shifting propulsion energy storage to onboard batteries [1]. Among the battery chemistries adopted in automotive applications, lithium-ion batteries (LIBs) remain the dominant choice due to their high energy density, long cycle life, and favorable power capability [2], [3]. However, LIB operation is intrinsically coupled with heat generation from electrochemical reactions and internal resistive losses. When heat is not effectively rejected, elevated cell temperature and strong spatial gradients accelerate aging, reduce available power, and may precipitate thermal runaway under abuse or extreme conditions [4]. For safety and durability, battery temperatures are commonly managed within a bounded operating window (often cited around 25–40 °C for typical performance targets), motivating the continued development of robust battery thermal management systems (BTMS) [5]-[7].

BTMS solutions span passive and active approaches, including air cooling, liquid cooling, phase-change materials (PCM), heat pipes, and hybrid combinations [8]-[13]. While air cooling is attractive for simplicity, liquid cooling typically provides higher heat removal capability and better temperature uniformity for high heat flux and high energy-density packs [14]. Within liquid-cooled BTMS, cold-plate liquid cooling has matured into one of the most prevalent indirect cooling architectures in practice, because it can be engineered to control both peak temperature and temperature non-uniformity while maintaining compact packaging [15], [16]. Recent reviews emphasize that modern cold-plate designs should not be assessed solely by peak temperature reduction; instead, multi-metric evaluation is increasingly expected, typically including maximum temperature Tmax, temperature uniformity indicators (e.g., ΔT or variance), and hydraulic penalties such as pressure drop Δp and pumping power [15], [16]. These metrics are also the basis for contemporary multi-objective optimization, where thermal performance improvements must be balanced against parasitic energy consumption and manufacturability constraints [15].

Accordingly, substantial research has focused on enhancing cold-plate hydrothermal performance through channel layout, flow distribution, and surface augmentation. Prior work has explored parallel-channel cold plates and the influence of coolant selection and channel count [17], as well as various geometric modifications (e.g., Tesla-valve-inspired inserts, mini-ribs, pin-fin arrays, dendritic or bionic channel motifs) to improve heat transfer and/or uniformity [18]-[23]. More recent studies further demonstrate that the field is moving from heuristic channel design toward systematic optimization frameworks. For example, topology-optimization and hybrid bionic–topology approaches have been used to derive channel networks that improve comprehensive thermal–hydraulic figures of merit, supported by combined numerical and experimental evidence [24]. Likewise, recent 3D topology-optimization studies explicitly target the trade-off between heat dissipation efficiency and flow resistance, often achieving substantial Δp reductions at the cost of modest changes in Tmax, reinforcing the need for balanced objective functions rather than single-metric conclusions [25]. Complementary to topology optimization, CFD-driven multi-objective optimization has also been applied to tune inlet geometries and non-uniform channel widths in order to reduce both pressure drop and thermal resistance while improving coolant distribution to hotspot regions [26].

In parallel, recent literature increasingly highlights that cold-plate performance at the module level is not governed solely by internal channel convection. The battery–cold-plate heat-transfer pathway frequently includes dominant

 EISSN: 2961-872X ● PISSN: 2961-8924 ● DOI: 10.56741/IISTR.esl.002023

resistances associated with conduction through cell casings and fixtures and, critically, the contact/interface thermal resistance introduced by thermal interface materials (TIMs), gaps, and assembly pressure. Thermal-resistance-network studies and cold-plate arrangement analyses show that contact resistance and interface design can materially influence the realized temperature field and the marginal benefit of channel-level enhancements [27]. Similarly, parametric investigations of cooling plate contact area demonstrate that changing the effective contact surface (and related geometric constraints) can alter Tmax, uniformity metrics, and hydraulic outcomes—again underscoring that module-level architecture must be evaluated as a coupled thermal–hydraulic system rather than a channel-only problem [28]. Recent engineering-focused studies also examine TIM thickness and distribution patterns for liquid-cooled packs to improve heat transfer robustness under realistic manufacturing non-uniformities [29].

Despite the breadth of channel-shape innovations and optimization studies, there remains a practical need for controlled, architecture-level comparisons that isolate the effect of flow-path configuration under consistent operating constraints and geometry scale relevant to battery modules. In particular, splitting the flow into multiple parallel paths through the use of two inlets and two outlets can plausibly reduce hydraulic resistance and mitigate maldistribution, but its net benefit must be demonstrated against key BTMS metrics (peak temperature, uniformity, and Δp/pumping cost) using consistent modeling assumptions and boundary conditions.

Therefore, this study presents a comparative numerical analysis of a single parallel-channel and a double parallel-channel (two-inlet/two-outlet) cold-plate configuration applied to a 7 Ah prismatic LiFePO4 battery module comprising three cells. Using a coupled CFD-based thermal analysis in ANSYS Fluent, the cooling performance is evaluated over coolant mass flow rates of 0.001–0.005 kg/s at a coolant inlet temperature of 25 °C and ambient temperature of 25 °C. The comparison focuses on (i) battery module maximum temperature, (ii) coolant pressure drop, and (iii) derived convective indicators (heat-transfer coefficient and Nusselt number), providing quantitative evidence on the thermal–hydraulic trade-offs introduced by the two flow-path architectures.

II. METHODS

A. Battery Specification, geometry and study design

This work conducts a numerical comparison of two liquid-cooled cold-plate architectures—(i) a single parallel-channel cold plate and (ii) a double parallel-channel cold plate with two inlets and two outlets—applied to a prismatic LiFePO4 battery module. The investigated cell is rated at 7 Ah with a maximum discharge current of 35 A. A battery module was formed by arranging three cells and connecting them at the tabs using busbars.

All 3D geometries were created in SolidWorks (Student Version). The prismatic cell dimensions are 63 mm (length) × 13 mm (width) × 116 mm (height). The cold plate is intended to collect heat from the battery module through the plate body and reject it by forced convection to the coolant. Aluminum was selected as the cold-plate material. For both designs, the channel width is 8 mm, the plate thickness is 2 mm, and the channel flow depth is 1 mm (see Fig. 1.).

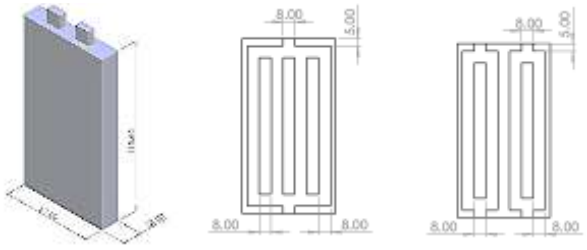

(a) (b) (c)

Fig. 1. Geometry and dimensions of the battery cell and cold-plate designs. (a) Prismatic LiFePO4 cell. (b) single parallel-channel cold plate; (c) double parallel-channel cold plate.

An array of three battery cells joined by busbars on the battery tab comprised a battery module. Figure 4 illustrates the incorporation of a cooling plate into battery cells for temperature management. In contrast, Figure 5 shows the direction of fluid flow through the two cooling plates. The direction of the fluid flow was designed to be in the opposite direction, producing equal cooling effects from the bottom and top of the battery.

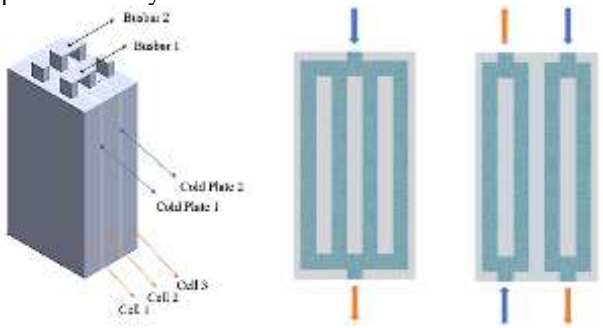

(a) (b) (c)

Fig. 2. Battery module assembly and coolant flow configurations. (a) Three-cell battery module integrated with cold plate; (b) flow direction for the single parallel-channel cold plate; (c) flow direction for the double parallel-channel cold plate.

To maintain comparable operating conditions between the two architectures, both cold-plate configurations were evaluated over the same overall coolant mass-flow range. For the double parallel-channel cold plate, the total mass flow rate was split equally between its two inlets; for example, a total of 0.001 kg/s was applied as 0.0005 kg/s at each inlet. The flow directions were arranged to provide opposite flow orientation across the plate so that cooling effects are distributed across the module. All simulations were performed using ANSYS Fluent 2023 R1 (Academic License).

B. Governing models and equations

Battery electro-thermal behavior in Fluent was modeled using the Multi-Scale Multi-Domain (MSMD) approach [30]. In this framework, coupled thermal and electrical fields are solved at cell scale using conservation relations for heat transfer and charge transport, as expressed in Eqs. (1)–(2).

$$\frac{\partial_\rho C_p T}{\partial t} - \nabla(k\nabla T) = \partial_+|\nabla\emptyset_+|^2 + \partial_-|\nabla\emptyset_-|^2 + \dot{q}_{ECh} + \dot{q}_{short} \quad (1)$$

$$\begin{cases} \nabla(\sigma_-\nabla\varphi_-) = (j_{ECh} - j_{short}) \\ \nabla(\sigma_+\nabla\varphi_+) = (j_{ECh} - j_{short}) \end{cases} \quad (2)$$

Here, σ_+, σ_- denote the effective electrical conductivity for the positive and negative electrodes (S/m), and φ_+, φ_- represent the potentials for the positive and negative electrodes (volt), respectively. Additionally, j_{ECh} and $\dot{q}_{ECh}$ signify the volumetric transfer rate of the current (A) and heat of the electrochemical reaction (J), whereas $j_{short}, \dot{q}_{short}$ indicates the current transfer rate (A) and heat generation rate due to the internal short circuit of the battery (J).

The volumetric current transfer rate is given by Eq. (3), which is a part of the formal model formulation.

$$j_{ECh} = aY[U - (\varphi_+ - \varphi_-)] \quad (3)$$

where a is the specific area of the electrode sheet (m^2) U, Y is the parameter model. U is a subcoordinate of the Depth of Discharge (DoD). DoD can be expressed by Eq. (4):

$$DoD = \frac{Vol}{3600 Q_{Ah}} \left(\int_0^t j \, dt \right) \quad (4)$$

where Q_{Ah} is the overall electrical battery capacity (Ah) and Vol is the battery volume (m^3). Fitting the experimental data curve yielded Y and U.

A semi-empirical electrochemical submodel based on the NTGK formulation is used to represent the transient electrochemical response within the MSMD framework [30]. The NTGK implementation uses fitted functions for the model parameters U and Y as functions of DoD and temperature (Eqs. (5)–(6)), where the constants are battery-specific and obtained by fitting to discharge characteristics.

$$\begin{cases} Y = \left(\sum_5^{n=0} a_n (DoD)^n\right) exp\left[-C_1\left(\frac{1}{T} - \frac{1}{T_{ref}}\right)\right] \\ U = \left(\sum_3^{n=3} b(DoD)^n\right) - C_2\left(T - T_{ref}\right) \end{cases} \quad (5)$$

$$\begin{cases} Y = \left(\sum_5^{n=0} a_n (DoD)^n\right) exp\left[-C_1\left(\frac{1}{T} - \frac{1}{T_{ref}}\right)\right] \\ U = \left(\sum_3^{n=3} b(DoD)^n\right) - C_2\left(T - T_{ref}\right) \end{cases} \quad (6)$$

Heat transfer and fluid flow in the cold plate are modeled using the governing equations for incompressible flow and energy transport [33,34]. The conservation of mass, momentum, and energy are given in Eqs. (7)–(9):

$$\frac{\partial(\rho)}{\partial t} + \nabla \cdot (\rho \vec{u}) = 0 \quad (7)$$

$$\frac{\partial(\rho \vec{u})}{\partial t} + \nabla \cdot (\rho \vec{u}\vec{u}) = -\nabla \mathrm{P} + \mu \nabla^2 \vec{u} \quad (8)$$

$$\frac{\partial(\rho C_p T)}{\partial t} + \nabla . \left(\rho C_p \vec{u} T\right) = \nabla . (\lambda \nabla \mathrm{T} \quad (9)$$

where P is the pressure (Pa), and u is the fluid velocity along the flow coordinates (m/s). ρ is the density (kg/m^3), C_p is the specific heat of the fluid (J/kgK), μ is the dynamic viscosity of the fluid $(Pa.s)$, and dan λ is the thermal conductivity of the fluid (W/mK).

Thermophysical properties for each material domain are listed in Table 1 and treated as constant over the investigated operating range.

TABLE I. THERMODYNAMIC PROPERTIES USED IN SIMULATIONS

Materials	Density (kg/m^3)	Specific Heat (J/kgK)	Thermal Conductivity (W/mK)
Water Cooling Fluid	998.2	4182	0.6
Aluminum Cold Plate	2719	871	202
$LiFePO_4$ Battery	2500	1000	3

C. Meshing strategy and numerical boundary conditions

The computational domain includes the battery module, cold plate(s), and coolant channels. The ambient temperature surrounding the external surfaces is set to 25 °C. Water is used as the coolant with an inlet temperature of 25 °C.

Boundary conditions were imposed as follows:

- Inlet: mass-flow inlet (varied over 0.001–0.005 kg/s total flow rate).
- Outlet: pressure outlet at 0 Pa gauge pressure.
- Flow model: laminar viscosity model.
- External convection: a free-convection boundary condition with a heat-transfer coefficient of 5 W/m²·°C applied at the exposed solid-domain surfaces.
- Battery operation: nominal capacity 7 Ah, discharge rate 5C, and discharge duration 720 s.

A hexahedral mesh was generated for the model (Fig. 3). The numerical solution employed a maximum of 30 iterations per time step/solution stage as configured in the study setup.

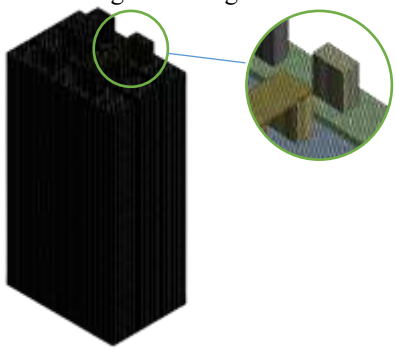

Fig. 3. Computational domain and mesh used in the CFD simulations. Representative hexahedral mesh for (a) battery module and (b) cold plate/channel domain (show refinement near channel walls and interfaces)

D. Mesh independence test

A mesh-independence assessment was performed using the single parallel-channel cold plate model to ensure solution stability. Six mesh sizes were tested: 1,133,238; 1,398,324; 1,526,861; 2,149,234; 2,425,020; and 3,637,372 elements (Fig. 4).

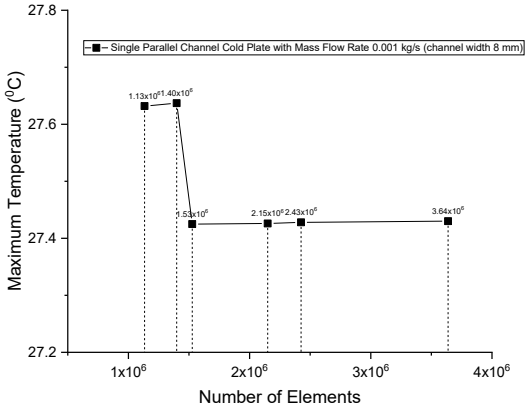

Fig. 4. Graph of Mesh Independent Test

The test condition used an ambient temperature of 25 °C, coolant inlet temperature 25 °C, mass flow rate 0.001 kg/s, and outlet pressure 0 Pa. Based on the stability of the predicted maximum battery-module temperature and the computational cost, the mesh with 2,425,020 elements was selected for subsequent simulations, yielding a maximum temperature of 27.428 °C under the mesh-test condition.

Validation was carried out using the research results [17], which was carried out with 4 channels and a width of 3 mm at an ambient temperature of 25 °C, a fluid temperature of 25 °C, and a mass flow rate of 0.001 kg/s. Fig. 5 shows a comparison of the results.

EISSN: 2961-872X ● PISSN: 2961-8924 ● DOI: 10.56741/IISTR.esl.002023

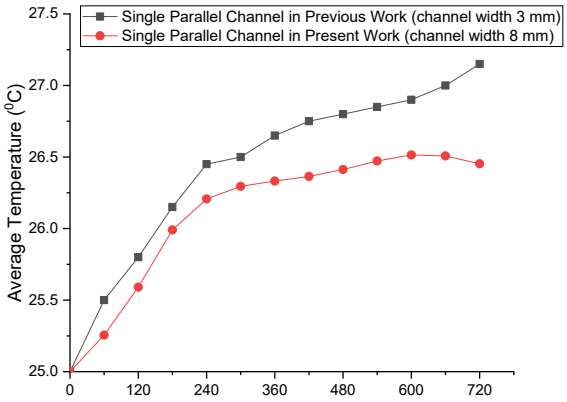

Fig. 5. Graph of average temperature of battery modules with single parallel channel cold plate present work (channel width 8 mm) and previous work (channel width 3 mm)

An inaccuracy of less than 10% indicated satisfactory agreement for validation. A larger channel width than that in the current study suggests a wider cooling surface area, which accounts for the temperature differential resulting from varied channel widths. The wider channel (8 mm) in the current study, compared to the narrower channel (3 mm) in the previous research, resulted in a generally lower average temperature for the battery module

E. Data reduction

Equation (10) can be used to calculate the pressure of the fluid as it enters and exits a cold plate with parallel channels.

$$\Delta p_w = p_{out} - p_{in} \tag{10}$$

where p_{out} is the outlet pressure (Pa), and p_{in} is the inlet pressure (Pa).

The heat removal capacity of the cooling fluid is expressed as a function of the battery cell volume in equation (11).

$$\dot{Q}_w = \dot{m}_w c_{p,w} \left(T_{w,out} - T_{w,in}\right) \tag{11}$$

where $\dot{Q}_w$ is the heat removed by the cooling fluid (W), $\dot{m}_w$ is the mass flow rate of the water (cooling fluid) (kg/s), $c_{p,w}$ is the specific heat of the water (J/kgK), $T_{w,out}$ is the outlet temperature of the water (℃) and $T_{w,in}$ is the inlet temperature of the water flow (℃).

The average heat transfer coefficient of water was determined using the following equation: (12):

$$h_w = \frac{\dot{Q}_w}{A_c[T_{bm,max} - (T_{w,out} + T_{w,in})/2]} \tag{12}$$

where h_w is the average heat transfer coefficient of the water $(W/m^2℃)$, $T_{bm,max}$ is the maximum temperature of the battery (℃) and A_c is the cooling area (m^2).

The Nusselt number of water can be calculated using Eq. (13):

$$Nu = h_w L_t / K_w \tag{13}$$

where L_t represents the characteristic length of the channel (m) and K_w denotes the thermal conductivity of the water.

III. Results and Discussions

Two distinct configurations of cold plates, specifically a single-parallel and double-parallel channel cold plate, were investigated to assess the effect of varying the mass flow rate of the cooling fluid on the temperature reduction in the LiFePO4 battery module. The Nusselt number, heat transfer coefficient, and pressure drop were among the cooling-fluid-related parameters examined in the investigation.

A. Effect of cooling fluid mass flow rate on battery module temperature conditions

The simulation was performed with a LiFePO4 battery module using two cold-plate models (channel width of 8 mm) as the thermal management system. The results showed that every change in the flow rate resulted in a decrease in temperature. Table II demonstrates that the double parallel plate exhibits greater effectiveness compared to the single parallel channel cold plate. The temperature was 0.10C lower at the lowest mass flow rate (0.001 kg/s) and 0.0480C lower at the highest mass flow rate (0.005 kg/s). The differences were statistically significant. An optimal mass flow rate of 0.005 kg/s produced the most significant reduction in the maximum temperature of the battery module for both cold-plate variants.

TABLE II. MAXIMUM BATTERY MODULE TEMPERATURE SIMULATION RESULTS

Mass Flow Rate [kg/s]	Battery Module Maximum Temperature [℃]	
	Single Parallel	*Double Parallel*
0.001	27.428	27.328
0.002	26.919	26.847
0.003	26.747	26.696
0.004	26.673	26.626
0.005	26.625	26.577

Fig. 6 presents a graphical representation of the relationship between mass flow rate and the efficacy of the two cold plate models in reducing the maximum temperature of the battery module.

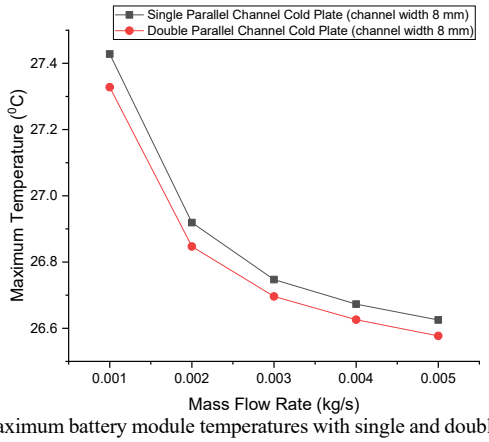

Fig. 6. Maximum battery module temperatures with single and double parallel channel cold plates (8 mm channel width) at different mass flow rates

Fig. 7 shows that the double parallel-channel cold plate effectively maintained the maximum temperature of the battery module at a mass flow rate of 0.001 kg/s. While both types of cold plates initially reduced the temperature of the battery module, the double parallel-channel cold plate ultimately demonstrated superior efficacy

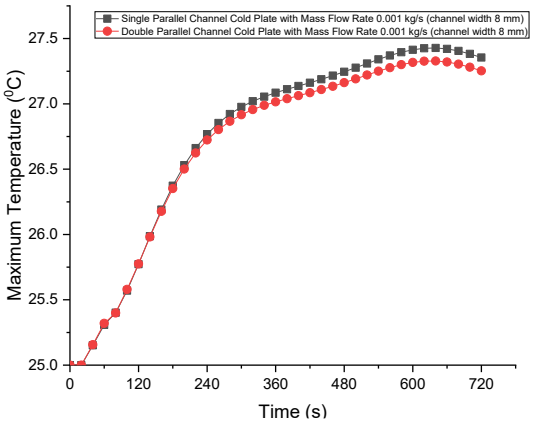

Fig. 7. Graph of maximum temperature of the battery module delivered with a single parallel channel cold plate (channel width 8 mm) and with a double parallel channel cold plate (channel width 8 mm) based on time at a mass flow rate of 0.001 kg/s.

Fig. 8 shows the maximum temperature under several conditions when the battery module contains a double parallel channel cold plate with varying mass flow rates. The maximum temperature of the battery module decreases as the mass flow rate increases

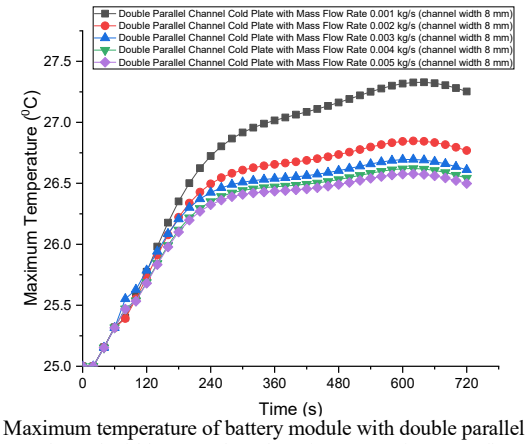

Fig. 8. Maximum temperature of battery module with double parallel channel cold plate (channel width 8 mm) based on time at varying mass flow rates.

Moreover, Fig. 9 shows that at any mass flow rate, battery cells 1 and 3 may reach higher maximum temperatures than those of battery cell 2. Battery cells 1 and 3 have only one side in contact with the cold plate, which explains why.

The double parallel channel cold plate demonstrated a more consistent cooling effect, particularly when the mass flow rate was 0.005 kg/s. For further insight into the maximum temperature variation among the battery cells, refer to Figure 10, which compares the battery cells in a battery module with a double parallel channel cold plate

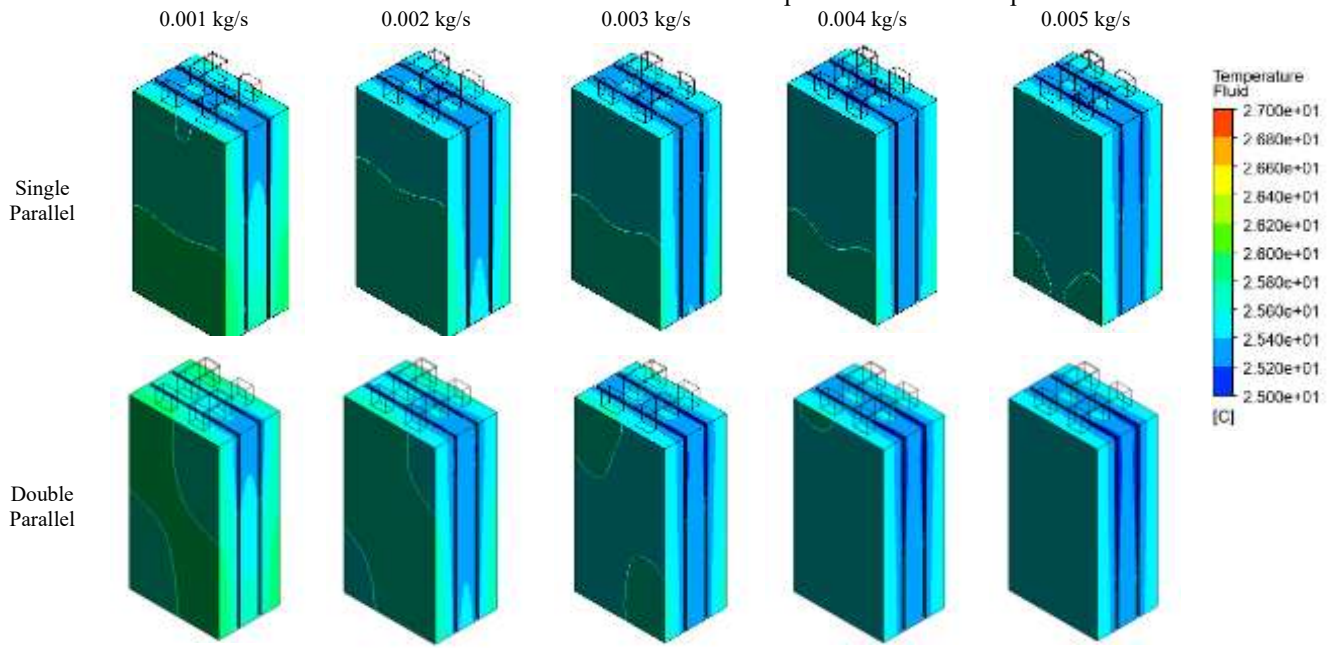

Fig. 9. Maximum temperature distribution of battery module with single parallel channel cold plate (channel width 8 mm) and double parallel channel cold plate (channel width of 8 mm) at varying mass flow rates

B. Effect of cooling fluid mass flow rate on cooling fluid conditions

Table III shows the variation in the characteristics of the cooling fluid water depending on the mass flow rate, as indicated by the temperature difference in the outflow of the cooling fluid. At the output, the cooling fluid temperature increases because of the heat transfer process of the battery module. The cooling fluid output increased at a lower temperature in a mass flow rate-dependent manner. Single- and double-parallel channel cold plates suffer from this problem.

The distribution of the cooling-fluid temperatures over the two cold plates is shown in Fig. 10.

TABLE III. MAXIMUM COOLING FLUID TEMPERATURE SIMULATION RESULTS

Mass Flow [kg/s]	Single Parallel Temperature [°C]		Double Parallel Temperature [°C]	
	Inlet	*Outlet*	*Inlet*	*Outlet*
0.001	25	26.433	25	26.352
0.002	25	25.776	25	25.695
0.003	25	25.538	25	25.470
0.004	25	25.416	25	25.351
0.005	25	25.340	25	25.279

According to the observations, the temperature of the cooling fluid is low at the beginning of the channel and high toward its conclusion. The double-parallel-channel cold plate also had a longer zone along the channel length where the cooling fluid temperature was lower.

EISSN: 2961-872X ● PISSN: 2961-8924 ● DOI: 10.56741/IISTR.esl.002023

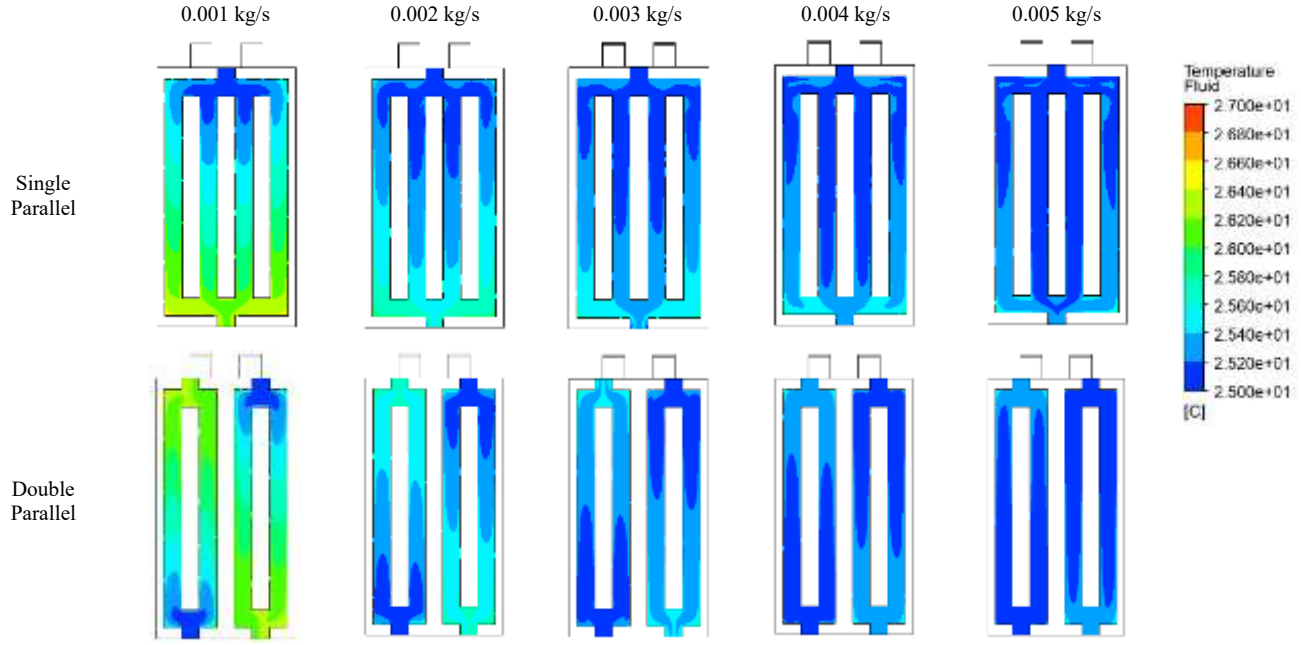

Fig. 10. Cooling fluid temperature distribution in a single parallel channel cold plate (channel width 8 mm) and double parallel channel cold plate (channel width 8 mm) at varying mass flow rates

Table IV presents the pressure drops occurring in both versions of the cold plates for various mass flow rates. Notably, the double-parallel channel cold plates exhibit a lower pressure drop. This difference occurs because, with a double parallel-channel cold plate, the mass flow rate is halved compared to that of single parallel-channel cold plates, despite being equal. Consequently, this division leads to reduced flow velocity, resulting in a diminished pressure drop. Fig. 11 shows a visual comparison of the cooling-fluid pressure reduction between the two types of cold plates.

In both cases of cold plates, the pressure drop of the cooling fluid increases with increasing mass flow rate. 61.388 Pa is the lowest pressure drop was 747.749 Pa and the maximum for the cooling fluid in a single parallel-channel cold plate. The cooling fluid of the double parallel channel cold plate has a pressure drop in the range of 38.466–290.785 Pa.

TABLE IV. COOLING FLUID PRESSURE DROP OF SIMULATION RESULTS

Mass Flow Rate (kg/s)	Pressure Drop (Pa)	
	Single Parallel	*Double Parallel*
0.001	61.388	38.466
0.002	164.368	84.108
0.003	315.092	140.88
0.004	508.88	210.161
0.005	747.749	290.785

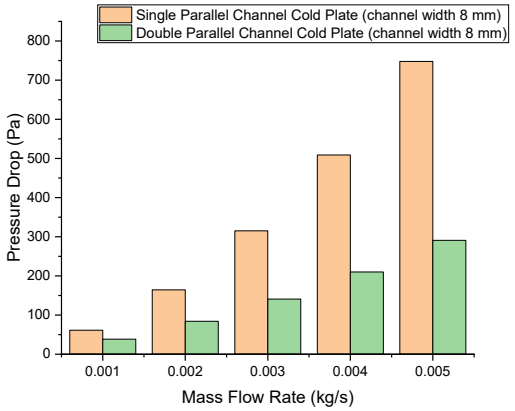

Fig. 11. Graph of pressure drop cooling fluid in single parallel channel cold plates (channel width 8 mm) and double parallel channel cold plates (channel width 8 mm) at varying mass flow rates.

Therefore, the pressure loss can be reduced by splitting the flow into two inlets. It follows that the pressure drop that occurs can be minimized using double parallel channel cold plates.

Fig. 12 shows the distribution of the cooling-fluid pressure on the two cold plates at varying mass flow rates. It can be seen that the fluid pressure has a high value at the beginning of the channel and then a low value at the end of the channel. This applies to both the cold plates.

Fig. 13 shows the pattern of the cooling fluid velocity in the two cold-plate models. The investigation revealed that the dual parallel channel cold plate exhibits very high fluid velocities and is evenly distributed in each of its dual channels, namely, left and right. The single parallel-channel cold plate had a slower cooling fluid circulation than its double-parallel-channel cold plate brother. Accordingly, the cooling fluid exit temperature of the double parallel channel cold plate was lower, as shown in Table IV. The maximum temperature of the battery module was lowered as a result of the double parallel channel cold plate installation.

C. Effect of Cooling Fluid Mass Flow Rate on the Heat Transfer Coefficient and Nusselt Number of Cooling Fluid

At cooling fluid flow rates of 0.001, 0.002, 0.003, 0.004, and 0.005 kg/s, the heat transfer coefficients of two cold plate configurations—single parallel channel and double parallel channel—were investigated. The results, illustrated in Fig. 15, indicate that the double parallel channel cold plate exhibits a lower heat transfer coefficient compared to the single parallel channel cold plate. Nevertheless, the double parallel configuration provides more effective cooling performance by reducing the battery module temperature more efficiently. This behavior is strongly influenced by the cooling fluid velocity and flow distribution within the channels.

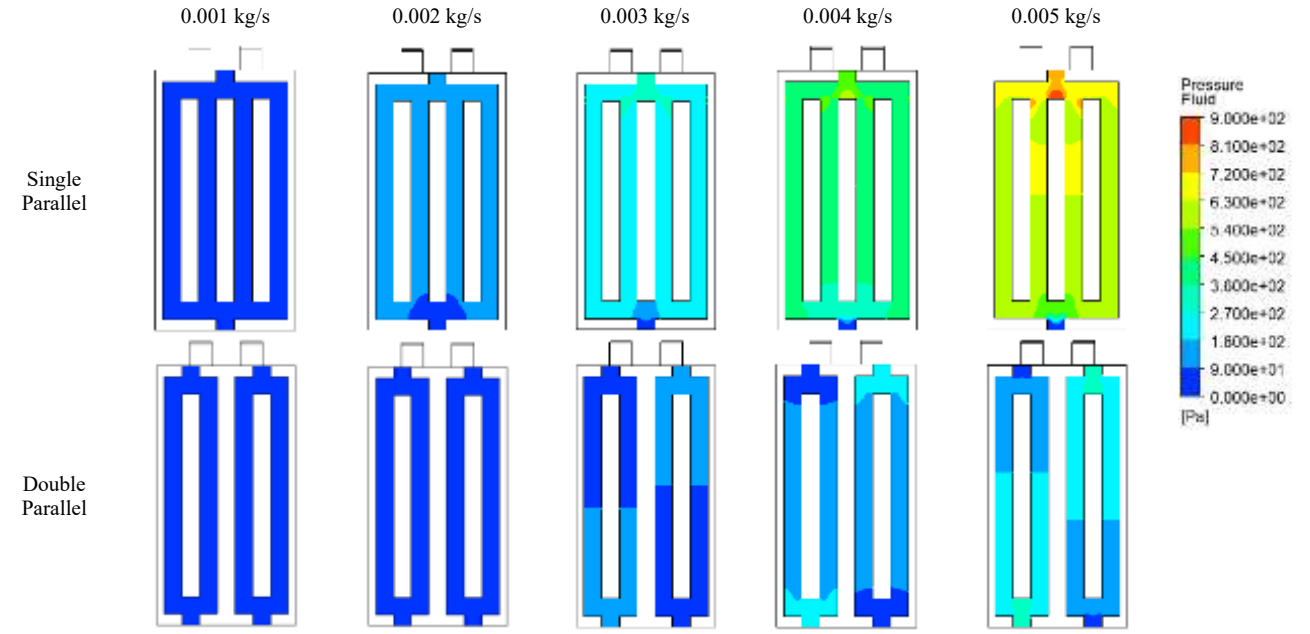

Fig. 12. Cooling fluid pressure distribution in single parallel channel cold plate (channel width 8 mm) and double parallel channel cold plate (channel width 8 mm) at varying mass flow rates

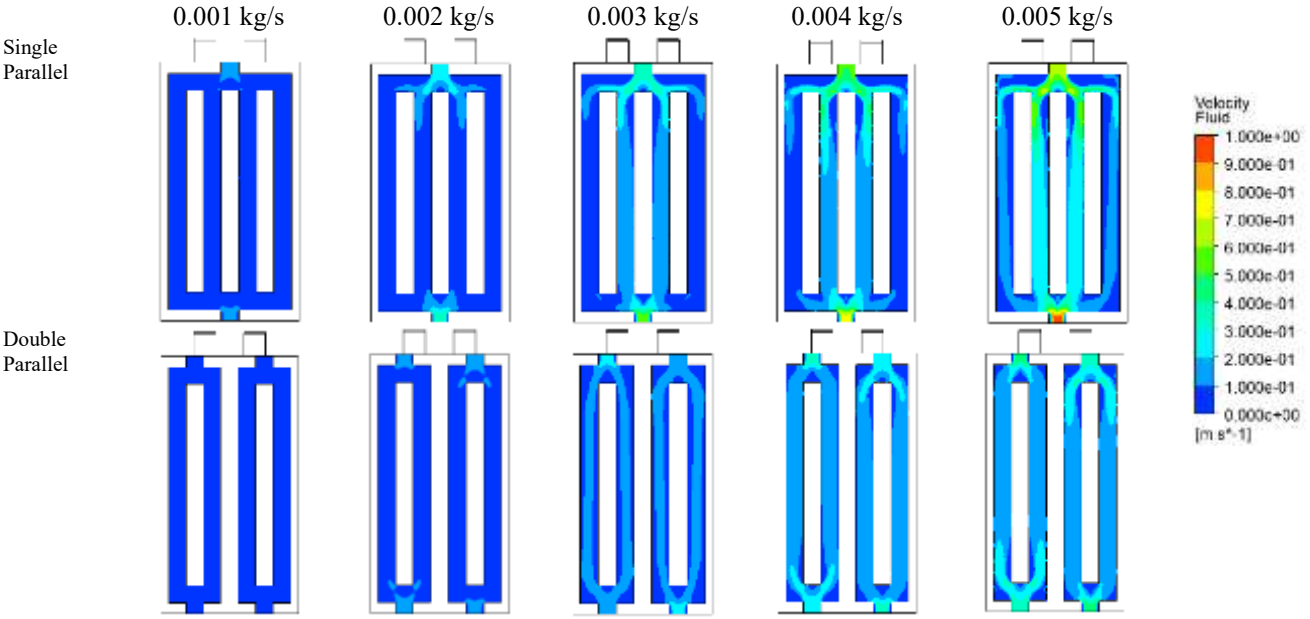

Fig. 13. Cooling fluid velocity distribution in a single parallel channel cold plate (channel width 8 mm) and double parallel channel cold plate (channel width 8 mm) at varying mass flow rates

In the double parallel channel design, the cooling fluid experiences lower temperature increases along several channel sections, leading to a smaller temperature rise at the fluid outlet compared to the single parallel channel model. According to Eq. 7, a greater temperature increase between the inlet and outlet fluid corresponds to a higher heat transfer value. Consequently, the single parallel channel cold plate achieves a higher calculated heat transfer coefficient because the coolant absorbs more heat, resulting in a larger outlet temperature rise. However, the lower outlet temperature rise observed in the double parallel channel design indicates that heat is distributed more evenly throughout the cooling plate, enabling more uniform thermal management of the battery module. In addition, increasing the mass flow rate improves the heat transfer coefficient in both cold plate configurations. Higher flow rates enhance coolant circulation and convective heat transfer, thereby improving the overall thermal performance of the cooling system. These findings suggest that although the single parallel channel cold plate yields a higher heat transfer coefficient, the double parallel channel cold plate offers superior temperature reduction and thermal uniformity, making it more suitable for maintaining stable battery operating conditions and preventing excessive temperature accumulation during operation.

EISSN: 2961-872X ● PISSN: 2961-8924 ● DOI: 10.56741/IISTR.esl.002023

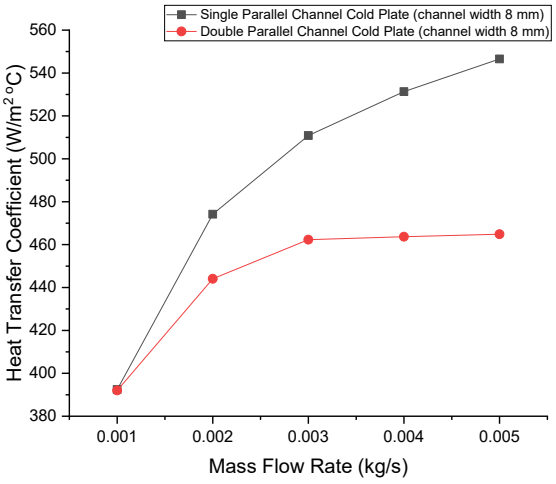

Fig. 14. Graph of heat transfer coefficient cooling fluid in single parallel channel cold plates (channel width 8 mm) and double parallel channel cold plates (channel width 8 mm) at varying mass flow rates.

In addition, the Nusselt number of the cooling fluid was investigated in both cold-plate models at the same flow rates of 0.001, 0.002, 0.003, 0.004, and 0.005 kg/s. According to the results, the cooling fluid in the cold plate with two parallel channels had a lower Nusselt number (Fig. 15). This is due to the cooling fluid's decreased heat transfer coefficient value in the double parallel channel cold plate, even when the channel length and thermal conductivity are both roughly constant. Furthermore, the mass flow rate can be increased to obtain a higher Nusselt value.

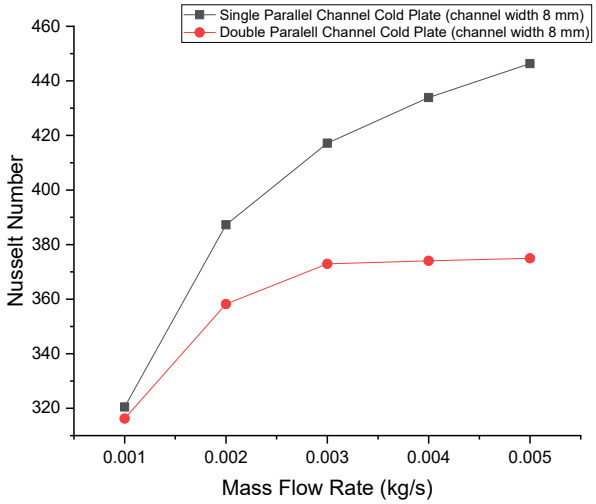

Fig. 15. Graph of Nusselt number cooling fluid in single parallel channel cold plates (channel width 8 mm) and double parallel channel cold plates (channel width 8 mm) at varying mass flow rates.

IV. Conclusion

In this study, the cooling performance of cold plates with two plate models, namely single parallel and double parallel channel cold plates, on prismatic-type LiFePO4 battery modules was investigated. The battery had a capacity of 7 Ah, with a maximum current of 35 A. The research was carried out numerically using the ANSYS 2023 R1 Academic License with mass flow rates of 0.001, 0.001, 0.002, 0.003, 0.004, and 0.005 kg/s. The study revealed that the double parallel channel cold plate outperformed the single parallel channel cold plate in reducing the maximum temperature of the battery, with a 0.1℃ advantage at a mass flow rate of 0.001 kg/s and a 0.048 ℃ advantage at a mass flow rate of 0.005 kg/s. Enhancing the mass flow rate improves the cooling capabilities of the battery module for both cold-plate designs. The pressure drop of the cooling fluid on a double parallel-channel cold plate is lower than that on a single parallel-channel cold plate. The heat transfer coefficient of the cooling fluid in the single parallel-channel cold plate was higher than that in the single-channel cold plate at each mass flow rate. This is because the fluid output temperature in the single parallel channel cold plate was higher than that in the double parallel channel cold plate. Therefore, the heat transfer value can be increased. Increasing the mass flow rate may lead to a higher heat-transfer coefficient for both cold plates. The Nusselt number of the cooling fluid in a single parallel-channel cold plate was higher than that in a double-parallel-channel cold plate. This is because the heat-transfer coefficient of the cooling fluid in a single parallel-channel cold plate is higher. Based on this research, to maintain the condition of the battery at an ideal temperature, a double parallel channel cold plate can be used.

For further research, it is necessary to investigate the use of double parallel cold plates in batteries that have a higher capacity to obtain higher temperatures so that the performance of the cold plates can be improved. The optimization of the channel width on the double parallel channel cold plate also needs to be performed. Additionally, it is necessary to investigate when the flow conditions are turbulent.

References

[1] Y. Lai, W. Wu, K. Chen, S. Wang, and C. Xin, "A compact and lightweight liquid-cooled thermal management solution for cylindrical lithium-ion power battery pack," *Int. J. Heat Mass Transf.*, vol. 144, p. 118581, Dec. 2019, doi: 10.1016/j.ijheatmasstransfer.2019.118581.

[2] F. Mohammadi and M. Saif, "A comprehensive overview of electric vehicle batteries market," *E-Prime - Adv. Electr. Eng. Electron. Energy*, vol. 3, p. 100127, Mar. 2023, doi: 10.1016/j.prime.2023.100127.

[3] M. Kiani, S. Omiddezyani, A. M. Nejad, M. Ashjaee, and E. Houshfar, "Novel hybrid thermal management for Li-ion batteries with nanofluid cooling in the presence of alternating magnetic field: An experimental study," *Case Stud. Therm. Eng.*, vol. 28, p. 101539, Dec. 2021, doi: 10.1016/j.csite.2021.101539.

[4] S. Shahid and M. Agelin-Chaab, "A review of thermal runaway prevention and mitigation strategies for lithium-ion batteries," *Energy Convers. Manag. X*, vol. 16, p. 100310, Dec. 2022, doi: 10.1016/j.ecmx.2022.100310.

[5] M. Akbarzadeh *et al.*, "A novel liquid cooling plate concept for thermal management of lithium-ion batteries in electric vehicles," *Energy Convers. Manag.*, vol. 231, p. 113862, 2021, doi: 10.1016/j.enconman.2021.113862.

[6] L. Jin *et al.*, "A novel hybrid thermal management approach towards high-voltage battery pack for electric vehicles," *Energy Convers. Manag.*, vol. 247, p. 114676, Nov. 2021, doi: 10.1016/j.enconman.2021.114676.

[7] W. Kong, K. Zhu, X. Lu, J. Jin, and M. Ni, "Enhancement of lithium-ion battery thermal management with the divergent-shaped channel cold plate," *J. Energy Storage*, vol. 42, p. 103027, Oct. 2021, doi: 10.1016/j.est.2021.103027.

[8] H. Xu, X. Zhang, G. Xiang, and H. Li, "Optimization of liquid cooling and heat dissipation system of lithium-ion battery packs of automobile," *Case Stud. Therm. Eng.*, vol. 26, p. 101012, Aug. 2021, doi: 10.1016/j.csite.2021.101012.

[9] Kausthubharam, P. K. Koorata, and N. Chandrasekaran, "Numerical investigation of cooling performance of a novel air-cooled thermal management system for cylindrical Li-ion battery module," *Appl. Therm. Eng.*, vol. 193, p. 116961, July 2021, doi: 10.1016/j.applthermaleng.2021.116961.

[10] M. M. El Idi, M. Karkri, and M. Abdou Tankari, "A passive thermal management system of Li-ion batteries using PCM composites: Experimental and numerical investigations," *Int. J. Heat Mass Transf.*, vol. 169, p. 120894, Apr. 2021, doi: 10.1016/j.ijheatmasstransfer.2020.120894.

[11] L. Wang, Y. Zhao, Z. Quan, and J. Liang, "Investigation of thermal management of lithium-ion battery based on micro heat pipe array," *J. Energy Storage*, vol. 39, p. 102624, July 2021, doi: 10.1016/j.est.2021.102624.

[12] S. Hekmat and G. R. Molaeimanesh, "Hybrid thermal management of a Li-ion battery module with phase change material and cooling water pipes: An experimental investigation," *Appl. Therm. Eng.*, vol. 166, p. 114759, Feb. 2020, doi: 10.1016/j.applthermaleng.2019.114759.

[13] H. Behi *et al.*, "A new concept of thermal management system in Li-ion battery using air cooling and heat pipe for electric vehicles," *Appl. Therm. Eng.*, vol. 174, p. 115280, June 2020, doi: 10.1016/j.applthermaleng.2020.115280.

[14] C. Wu, Z. Wang, Y. Bao, J. Zhao, and Z. Rao, "Investigation on the performance enhancement of baffled cold plate based battery thermal management system," *J. Energy Storage*, vol. 41, p. 102882, Sept. 2021, doi: 10.1016/j.est.2021.102882.

[15] C. Wu *et al.*, "A review on the liquid cooling thermal management system of lithium-ion batteries," *Appl. Energy*, vol. 375, p. 124173, Dec. 2024, doi: 10.1016/j.apenergy.2024.124173.

[16] Z. Qianqian *et al.*, "Thermal management of lithium-ion batteries: from single cooling to hybrid cooling," Jan. 2026, doi: 10.1039/D5RA08014B.

[17] K. Monika, C. Chakraborty, S. Roy, S. Dinda, S. A. Singh, and S. P. Datta, "An improved mini-channel based liquid cooling strategy of prismatic LiFePO4 batteries for electric or hybrid vehicles," *J. Energy Storage*, vol. 35, p. 102301, Mar. 2021, doi: 10.1016/j.est.2021.102301.

[18] K. Monika, C. Chakraborty, S. Roy, R. Sujith, and S. P. Datta, "A numerical analysis on multi-stage Tesla valve based cold plate for cooling of pouch type Li-ion batteries," *Int. J. Heat Mass Transf.*, vol. 177, p. 121560, Oct. 2021, doi: 10.1016/j.ijheatmasstransfer.2021.121560.

[19] W. Jiang, J. Zhao, and Z. Rao, "Heat transfer performance enhancement of liquid cold plate based on mini V-shaped rib for battery thermal management," *Appl. Therm. Eng.*, vol. 189, p. 116729, May 2021, doi: 10.1016/j.applthermaleng.2021.116729.

[20] R. Zhao *et al.*, "Performance analysis and optimization of a novel cooling plate with non-uniform pin-fins for lithium battery thermal management," *Appl. Therm. Eng.*, vol. 194, p. 117022, July 2021, doi: 10.1016/j.applthermaleng.2021.117022.

[21] Y. Fan, Z. Wang, and T. Fu, "Multi-objective optimization design of lithium-ion battery liquid cooling plate with double-layered dendritic channels," *Appl. Therm. Eng.*, vol. 199, p. 117541, Nov. 2021, doi: 10.1016/j.applthermaleng.2021.117541.

[22] J. Wang, X. Liu, F. Liu, Y. Liu, F. Wang, and N. Yang, "Numerical optimization of the cooling effect of the bionic spider-web channel cold plate on a pouch lithium-ion battery," *Case Stud. Therm. Eng.*, vol. 26, p. 101124, Aug. 2021, doi: 10.1016/j.csite.2021.101124.

[23] B. Li, W. Wang, S. Bei, and Z. Quan, "Analysis of Heat Dissipation Performance of Battery Liquid Cooling Plate Based on Bionic Structure," *Sustainability*, vol. 14, no. 9, May 2022, doi: 10.3390/su14095541.

[24] S. Zhan, L. Liang, Z. Li, C. Yu, and F. Wang, "Topology optimization of liquid cooling plate for lithium battery heat dissipation based on a bionic leaf-vein structure," *Int. J. Heat Mass Transf.*, vol. 231, p. 125898, Oct. 2024, doi: 10.1016/j.ijheatmasstransfer.2024.125898.

[25] Z. Gu, B. Zhang, L. Zhou, Z. Chen, D. Zhao, and A. Lou, "Topology optimization on heat dissipation of liquid cooling plates for lithium-ion batteries," *Case Stud. Therm. Eng.*, vol. 77, p. 107505, Jan. 2026, doi: 10.1016/j.csite.2025.107505.

[26] W. Yin *et al.*, "Multi-objective CFD-based optimization of cold plates with non-uniform inlet and channel geometries," *Case Stud. Therm. Eng.*, vol. 76, p. 107432, Dec. 2025, doi: 10.1016/j.csite.2025.107432.

[27] Z. An *et al.*, "Optimization design of lithium-ion battery thermal management system based on thermal resistance network analysis and cold plate arrangement," *Therm. Sci. Eng. Prog.*, vol. 68, p. 104335, Dec. 2025, doi: 10.1016/j.tsep.2025.104335.

[28] S. Birinci, M. Albayrak, B. Sarper, M. Y. Yazici, M. Saglam, and O. Aydin, "Effect of cooling plate contact area and flow rate on the performance of liquid-cooled cylindrical lithium-ion battery pack," *Appl. Therm. Eng.*, vol. 279, p. 127708, Nov. 2025, doi: 10.1016/j.applthermaleng.2025.127708.

[29] M. K, M. Jahagirdar, and M. S. Kumbhar, "Optimization and Evaluation of Thermal Interface Material Thickness and Distribution Patterns for Improved Heat Transfer in Liquid-Cooled Battery Pack," SAE International, Jan. 2026. doi: 10.4271/2026-26-0432.

[30] S. S. Madani, M. J. Swierczynski, and S. K. Kær, "The discharge behavior of lithium-ion batteries using the Dual-Potential Multi-Scale Multi-Dimensional (MSMD) Battery Model," in *2017 Twelfth International Conference on Ecological Vehicles and Renewable Energies (EVER)*, Apr. 2017, pp. 1–14. doi: 10.1109/EVER.2017.7935915.

 EISSN: 2961-872X ● PISSN: 2961-8924 ● DOI: 10.56741/IISTR.esl.002023